# High-order adaptive optics requirements for direct detection of extrasolar planets: Application to the SPHERE instrument

T. Fusco, G. Rousset, J.-F. Sauvage, C. Petit, J.-L. Beuzit, K. Dohlen, D. Mouillet, J. Charton, M. Nicolle, M. Kasper, et al.

# High-order adaptive optics requirements for direct detection of extrasolar planets: Application to the SPHERE instrument

**T. Fusco[1], G. Rousset[2,1], J.-F Sauvage[1], C. Petit[1], J.-L Beuzit[3], K. Dohlen[4], D. Mouillet[5], J. Charton[3], M. Nicolle[1], M. Kasper[6] , P. Baudoz[2], and P. Puget[2]**

[1] *ONERA, Optics Department, BP 72, F-92322 Chatillon, France*
[2] *LESIA, Observatoire de Paris, 5 Place Jules Janssen 92195 Meudon, France*
[3] *LAOG, Observatoire de Grenoble, BP 53, F-38041 Grenoble, France*
[4] *LAM, Observatoire de Marseille, BP 8, F-13376 Marseille, France*
[5] *Observatoire Midi-Pyrénées, 57 Avenue d'Azereix, BP 826, F-65008 Tarbes, France*
[6] *ESO, Karl-Schwarzschild-Straße 2, Garching, D-85748 Germany*

*thierry.fusco@onera.fr*

**Abstract:** The detection of extrasolar planets implies an extremely high-contrast, long-exposure imaging capability at near infrared and probably visible wavelengths. We present here the core of any Planet Finder instrument, that is, the extreme adaptive optics (XAO) subsystem. The level of AO correction directly impacts the exposure time required for planet detection. In addition, the capacity of the AO system to calibrate all the instrument static defects ultimately limits detectivity. Hence, the extreme AO system has to adjust for the perturbations induced by the atmospheric turbulence, as well as for the internal aberrations of the instrument itself. We propose a feasibility study for an extreme AO system in the frame of the SPHERE (Spectro-Polarimetry High-contrast Exoplanet Research) instrument, which is currently under design and should equip one of the four VLT 8-m telescopes in 2010.



**OCIS codes:** (010.1080) Adaptive optics; (120.1880) Detection

## References and links

1. J.-L. Beuzit, D. Mouillet, C. Moutou, K. Dohlen, P. Puget, T. Fusco, and A. Boccaletti, "A planet finder instrument for the VLT," in *Proceedings of IAU Colloquium 200, Direct Imaging of Exoplanets: Science & Techniques* (Cambridge University Press, 2005), pp. 317–323.
2. R. Racine, G. A. Walker, D. Nadeau, and C. Marois, "Speckle noise and the detection of faint companions," Pub. Astron. Soc. Pacific **112**, 587–594 (1999).
3. R. Lenzen, L. Close, W. Brandner, M. Hartung, and B. Biller, "NACO-SDI: A novel simultaneous differential imager for the direct imaging of giant extra-solar planets," in *Proceedings of Science with Adaptive Optics*, W. Brandner and M. Kasper, eds. (Springer-Verlag, 2004), pp. 47–50.
4. J.-F. Sauvage, L. Mugnier, T. Fusco, and G. Rousset "Post processing of differential images for direct extrasolar planet detection from the ground," in *Advances in Adaptive Optics II*, Proc. SPIE **6272**, pp. 753–763.
5. H. M. Schmid, J.-L. Beuzit, M. Feldt, D. Gisler, R. Gratton, T. Henning, F. Joos, M. Kasper, R. Lenzen, D. Mouillet, C. Moutou, A. Quirrenbach, D. M. Stam, C. Thalmann, J. Tinbergen, C. Verinaud, R. Waters, and R. Wolstencroft, "Search and investigation of extra-solar planets with polarimetry," in *Proceedings of IAU Colloquium 200, Direct Imaging of Exoplanets: Science & Techniques* (Cambridge University Press, 2005), pp. 165–170.
6. R. Soummer, "Apodized pupil Lyot coronagraphs for arbitrary telescope apertures," Astrophys. J. **618**, 161-164 (2005).

#69303 - $15.00 USD Received 23 March 2006; revised 20 June 2006; accepted 20 June 2006

7. A. Boccaletti, P. Riaud, P. Baudoz, J. Baudrand, D. Rouan, D. Gratadour, F. Lacombe, and A.-M. Lagrange, "The four-quadrant phase-mask coronagraph IV. First light at the very large telescope," Pub. Astron. Soc. Pacific **116**, 1061–1071 (2004).
8. J.-F. Sauvage, T. Fusco, G. Rousset, C. Petit, A. Blanc, B. Neichel, and J.-L. Beuzit, "Fine calibration and pre-compensation of non-common path aberrations for high performance AO system," in *Astronomical Adaptive Optics Systems and Applications II*, R. K. Tyson and M. Lloyd-Hart, eds., Proc. SPIE **5903**, 88–95 (2005).
9. F. Rigaut, J.-P. Véran, and O. Lai, "Analytical model for Shack-Hartmann-based adaptive optics system," Proc. SPIE **3353**, 1038–1048 (1998).
10. L. Jolissaint and J.-P. Véran, "Fast computation and morphologic interpretation of the Adaptive Optics Point Spread Function," in *Beyond Conventional Adaptive Optics*, E. Vernet, R. Ragazzoni, S. Esposito, and N. Hubin, eds., Vol. 58 of European Southern Observatory Conference and Workshop Proceedings (ESO, 2002), pp. 201–205.
11. R. Conan, T. Fusco, G. Rousset, D. Mouillet, J.-L. Beuzit, M. Nicolle, and C. Petit, "Modeling and analysis of XAO systems. Application to VLT-Planet Finder," in *Advancements in Adaptive Optics*, Proc. SPIE **5490**, 602–608 (2004).
12. C. Robert, J.-M. Conan, V. Michau, T. Fusco, and N. Vedrenne, "Scintillation and phase anisoplanatism in Shack–Hartmann Wavefront Sensing," J. Opt. Soc. Am. A **23**, 613–624 (2006).
13. O. Guyon, "Limits of adaptive optics for high-contrast imaging," Astrophys. J. **629**, 592–614 (2005).
14. F. Roddier and C. Roddier, "NOAO Infrared Adaptive Optics Program II: modeling atmospheric effects in adaptive optics systems for astronomical telescopes," in *Advanced Technology Optical Telescopes III*, L. D. Barr, ed., Proc. SPIE **628**, 298–304 (1986).
15. E. Masciadri, M. Feldt, and S. Hippler, "Scintillation effects on a high-contrast imaging instrument for direct extrasolar planets' detection," Astrophys. J. **613**, 572–579 (2004).
16. F. Mahé, V. Michau, G. Rousset, and J.-M. Conan, "Scintillation effects on wavefront sensing in the Rytov regime," in *Propagation through the Atmosphere IV*, M. Roggemann, ed., Proc. SPIE **4125**, 77–86 (2000).
17. C. Cavarroc, A. Boccaletti, P. Baudoz, T. Fusco, and D. Rouan, "Fundamental limitations on Earth-like planet detection with extremely large telescopes," Astron. Astrophys. **447**, 397–403 (2006).
18. P.-Y. Madec, "Control techniques," in *Adaptive Optics in Astronomy*, F. Roddier, ed. (Cambridge University Press, 1999), pp. 131–154.
19. C. Petit, F. Quiros-Pacheco, J.-M. Conan, C. Kulcsar, H.-F. Raynaud, T. Fusco, and G. Rousset, "Kalman Filter based control loop for Adaptive Optics," in *Advancements in Adaptive Optics*, Proc. SPIE **5490**, 1414–1425 (2004).
20. E. Gendron and P. Léna, "Astronomical adaptive optics I. Modal control optimization," Astron. Astrophys. **291**, 337–347 (1994).
21. L. A. Poyneer and B. Macintosh, "Spatially filtered wave-front sensor for high-order adaptive optics," J. Opt. Soc. Am. A **21**, 810–819 (2004).
22. T. Fusco, M. Nicolle, G. Rousset, V. Michau, J.-L. Beuzit, and D. Mouillet, "Optimisation of Shack-Hartmann-based wavefront sensor for XAO system," in *Advancements in Adaptive Optics*, Proc. SPIE **5490**, 1155–1166 (2004).
23. T. Fusco, C. Petit, G. Rousset, J.-M. Conan, and J.-L. Beuzit, "Closed-loop experimental validation of the spatially filtered Shack-Hartmann concept," Opt. Lett. **30**, 1255–1257 (2005).
24. M. Nicolle, T. Fusco, G. Rousset, and V. Michau, "Improvement of Shack-Hartmann wavefront sensor measurement for extreme adaptive optics," Opt. Lett. **29**, 2743–2745 (2004).
25. T. Fusco, G. Rousset, and A. Blanc, "Calibration of AO system. Application to NAOS-CONICA," in *Science with Adaptive Optics*, W. Brandner and M. Kasper, eds. (Springer-Verlag, 2004), pp. 103–107.
26. M. Kasper, E. Fedrigo, D. P. Looze, H. Bonnet, L. Ivanescu, and S. Oberti, "Fast calibration of high-order adaptive optics systems," J. Opt. Soc. Am. A **21**, 1004–1008 (2004).
27. A. Blanc, T. Fusco, M. Hartung, L. M. Mugnier, and G. Rousset, "Calibration of NAOS and CONICA static aberrations. Application of the phase diversity technique," Astron. Astrophys. **399**, 373–383 (2003), URL mailto:mugnier@onera.fr.
28. M. S. Robbins and B. J. Hadwen, "The noise performance of electron multiplying charge coupled device," IEEE Trans. Electron. Devices **50**, 1227–1232 (2003).

## 1. Introduction

Direct detection and spectral characterization of exoplanets is one of the most exciting but also one of the most challenging areas in the current astronomy. In that framework, the SPHERE (Spectro-Polarimetry High-contrast Exoplanet Research) instrument is currently under design and should equip one of the four 8-m telescopes of the European Southern Observatory Very Large Telescope (ESO VLT) at Paranal (Chile). The main scientific objective of SPHERE [1] is

#69303 - $15.00 USD Received 23 March 2006; revised 20 June 2006; accepted 20 June 2006

the direct detection of photons coming from giant extrasolar planets (between 1 and 20 Jupiter masses). Any detection will then be followed by a first characterization of the planet atmosphere (clouds, dust content, methane, water absorption...). In addition, the survey of an extended number of stars (typically a few hundreds) is mandatory for performing meaningful statistical studies. Such extremely challenging scientific objectives directly translate into a relatively complex high-contrast instrument. Coronagraphic and smart imaging capabilities are essential for reaching the high contrast (close to the optical axis) required for direct extrasolar planet detection. From the ground, the core of any high-contrast instrument is an extreme adaptive optics (XAO) system. Such a system must be capable of making corrections for the perturbations induced by the atmospheric turbulence as well as for the internal aberrations of the instrument itself.

In the following sections, we mainly focus on the main AO loop design. After a brief description of the SPHERE instrument in Section 2, a presentation of the coronagraphic image profile is posed, and its impacts on system performance are highlighted. The global error budget of the AO system is presented in Section 3, and details of each term are given in Sections 4 to 9. After the required trade-offs in terms of system design, a global presentation of the SPHERE extreme AO system (SAXO) is proposed in Section 10.

## 2. SPHERE and SAXO

The SPHERE system aims at detecting extremely faint sources (giant extrasolar planets) in the vicinity of bright stars. Such a challenging goal requires the use of a very-high-order performance AO system, a coronagraphic device to cancel out the flux coming from the star itself, and smart focal plane techniques to calibrate any coronagraph imperfections and residual uncorrected turbulent or static wavefronts.

The detection limit for the SPHERE instrument is $10^{-6}$ (i.e., 15 magnitudes between star and the planet) with a goal around $10^{-8}$. There is no direct link between the AO system performance and the final detectivity of the instrument; nevertheless, the impact of AO on the final performance is related to the performance of the coronagraph. A better AO correction leads to a better coronagraph extinction and therefore leads to the following improvements in system performance:

- a reduction of the photon and flat-field noises (i.e., a gain in Signal-to-Noise Ratio for a given integration time),
- a reduction of the pinned speckle (through the reduction of airy pattern intensity due to the coronagraph optimization).

These reductions are important from the global system performance point of view, and the optimization of the coronagraph rejection is a main goal of the SPHERE system. It of course requires the use and the optimization of an XAO system, as presented in the following. Nevertheless, the ultimate detection limit will be achieved through an extreme control of system internal defects (noncommon path aberrations (NCPAs), optical axis decentering, vibrations, coronagraph and imaging system imperfections, and so on). This ultimate control will also be partially ensured by the AO system through the use of additional devices in the AO concept (see Sections 8 and 9).

To meet the requirements (and hopefully the goal) in terms of detection, the proposed design of SPHERE is divided into four subsystems, namely, the common path optics and three science channels. The common path includes pupil-stabilizing foreoptics (tip-tilt and derotator) where insertable polarimetric half-wave plates are also provided, the SAXO XAO system with a visible wavefront sensor, and near infrared (NIR) coronagraphic devices in order to feed the infrared dual-imaging spectrograph (IRDIS) and the integral field spectrograph (IFS) with a

#69303 - $15.00 USD Received 23 March 2006; revised 20 June 2006; accepted 20 June 2006

highly stable coronagraphic image in the NIR. The three scientific channels gather complementary instrumentation to maximize the probability of exoplanet detection and to give us access to a large range of wavelengths and information (e.g., imaging, spectra, polarization).

The first instrument is an imaging camera (IRDIS). It is based on the principle of differential imaging initially proposed by R. Racine [2] and recently demonstrated on the VLT NACO instrument with the SDI device [3]. The idea is to record simultaneously two images at two close wavelengths. Assuming that there is a spectral feature in the object (absorption in one of the wavelengths), it is therefore possible to distinguish the speckle pattern (which has the same contribution at the two wavelengths) and the faint object. This distinction can be done by using a simple subtraction of the two images or considering more clever signal processing approaches [4].

The second focal plane instrument will be an IFS working from 0.95 $\mu$m to 1.7 $\mu$m and providing low spectral resolution (R $\sim$ 30) over a limited, 3" $\times$ 3", field of view. The last scientific channel contains a visible dual-imaging polarimeter (ZIMPOL), working between 0.65 $\mu$m and 0.95 $\mu$m. Due to its innovative lock-in technique [5], it can achieve polarimetric precisions better than $10^{-5}$ on a localized signal measured differentially against a smooth background. ZIMPOL shares the visible channel with the wavefront sensor and includes its own coronagraphic system.

The concept behind this very challenging instrument is illustrated in Fig. 1, where the common NIR-Vis beam is indicated in orange, the exclusively NIR beam is indicated in red, and the exclusively Vis beam is indicated in blue.

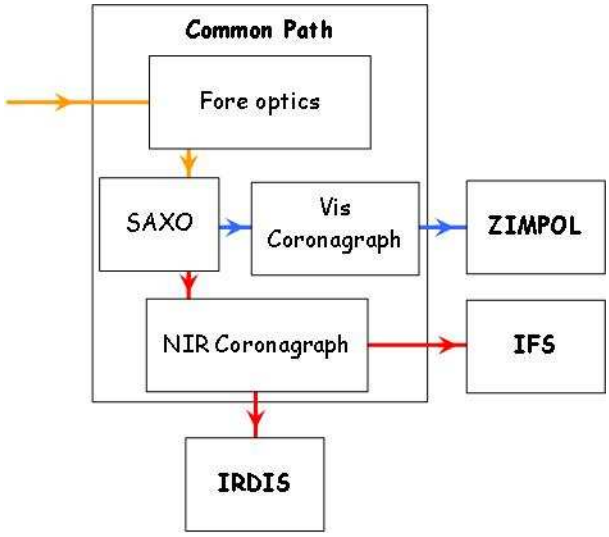


Fig. 1. Global concept of the SPHERE instrument, indicating the four subsystems and the main functionalities within the common path subsystem. Optical beams are indicated in red for NIR, blue for Vis, and orange for common path.

The foreoptics system, originally dedicated to pupil stabilization (lateral and rotational), also accommodates two insertable half-wave plates (required during ZIMPOL observations) and a polarizer for its calibration. A photon-sharing scheme has been agreed on between IRDIS and IFS, thus allowing IFS to exploit the NIR range up to the *J*-band. The *H*-band, optimal for the dual-band imaging (DBI) mode, is required for IRDIS during the main observation program. This multiplexing optimizes observational efficiency. However, the additional requirements in

#69303 - $15.00 USD Received 23 March 2006; revised 20 June 2006; accepted 20 June 2006

terms of broadband Atmospheric dispersion (ADC) and coronagraph efficiencies still need to be fully investigated.

The instrument will be mounted on the Nasmyth platform rather than directly attached to the telescope Nasmyth rotator. Indeed, this one is not adapted for carrying the full charge of the instrument bench. All the subsystems will be mounted onto the bench, which is likely to be actively damped by a pneumatic servo-controlled system and equipped with a dust cover.

The extreme AO system (SAXO) is the core of the SPHERE instrument, and is essential for reaching the extremely high contrast requirements. In this framework, the SAXO must fulfill the following three high-level requirements:

- Ensure the measurement and correction of the turbulent phase perturbations of the telescope and system common optics aberrations and of the NCPAs (main AO loop);
- Ensure an extremely high stability (at low temporal frequency) of the optical axis at the level of the coronagraphic mask [auxiliary sensor (AS)];
- Ensure the measurement and the correction of any pupil motion [pupil motion sensor (PMS)].

In keeping with the three main high-level requirements and in close collaboration with astronomers, we have performed a detailed optimization of the SAXO system, which is summarized hereafter.

## 3. Coronagraphic profile and detection signal-to-noise ratio

The first and critical point to be addressed for any AO system optimization is the performance estimation parameter. Unlike classical AO systems, residual variance and Strehl ratio are not sufficient anymore for optimizing the system and deriving the pertinent trade-offs. They have to be replaced by a more accurate parameter that can provide information on the coronagraphic image shape in the focal plane. During the past few years, a large number of coronagraphic devices have been proposed, ranging from modified Lyot concepts (with apodization for instance [6]) to interferometric devices such as the four quadrants coronagraph [7]. Each approach has its own advantages and drawbacks, and it is likely that more than one device will be implemented in the SPHERE instrument. In any case, the purpose of the coronagraph is to remove the coherent light coming from the on-axis guide star (GS). Therefore one can analytically define a "perfect coronagraph" using the following equations:

$$C_{res}(\rho) = \langle \left| \mathrm{FT}\left[ P(r)A(r)e^{i\varphi_{res}(r)} - \sqrt{Ec}\,P(r) \right] \right|^2 \rangle. \tag{1}$$

$C_{res}(\rho)$ corresponds to the image intensity in the focal plane after the coronagraphic process. $\rho$ stands for the focal plane position, $r$ for the pupil plane coordinates, and $\langle . \rangle$ for a statistical average; and, with $A(r)$ the wavefront amplitude, $\varphi_{res}(r)$ the residual phase after AO correction, $P(r)$ the pupil function and $Ec$ the short exposure coherent energy defined as follows:

$$Ec = \exp\left[ -\sigma_{\varphi}^2 - \sigma_{\log(A)}^2 \right], \tag{2}$$

with

$$\sigma_{\varphi}^2 = \frac{1}{\mathscr{S}} \left\{ \int_{\mathscr{S}} \left( \varphi(r') - \left( \frac{1}{\mathscr{S}} \int_{\mathscr{S}} \varphi(r) dr \right) \right)^2 dr' \right\} \tag{3}$$

$$\sigma_{\log(A)}^2 = \frac{1}{\mathscr{S}} \left\{ \int_{\mathscr{S}} \left( \log\left[A(r')\right] - \left( \frac{1}{\mathscr{S}} \int_{\mathscr{S}} \log\left[A(r)\right] dr \right) \right)^2 dr' \right\}. \tag{4}$$

#69303 - $15.00 USD Received 23 March 2006; revised 20 June 2006; accepted 20 June 2006

It is interesting to note that when $Ec = 1$, i.e., when all the phase and amplitude effects have been corrected, all the light coming from the star has been canceled out. When only a partial correction is performed, the coherent peak is removed and only the incoherent light (the residual uncorrected speckles) remains. In that case, it is easy to show that, as a first approximation (first order expansion) the coronagraphic image intensity is proportional to the residual phase power spectral density:

$$C_{res}(\rho) \propto \langle |\mathrm{FT}[\varphi_{res}(r)]|^2 \rangle. \tag{5}$$

This is illustrated in Fig. 2 where both classical and coronagraphic images (cut off along the x-axis) are plotted in the case of a 41 x 41 actuator system with a 1.5 kHz sampling frequency. A sufficiently bright GS is considered, so the noise measurement effects can be disregarded. The average wind speed value is 12.5 m/s, and the seeing is 0.85 arcsec.

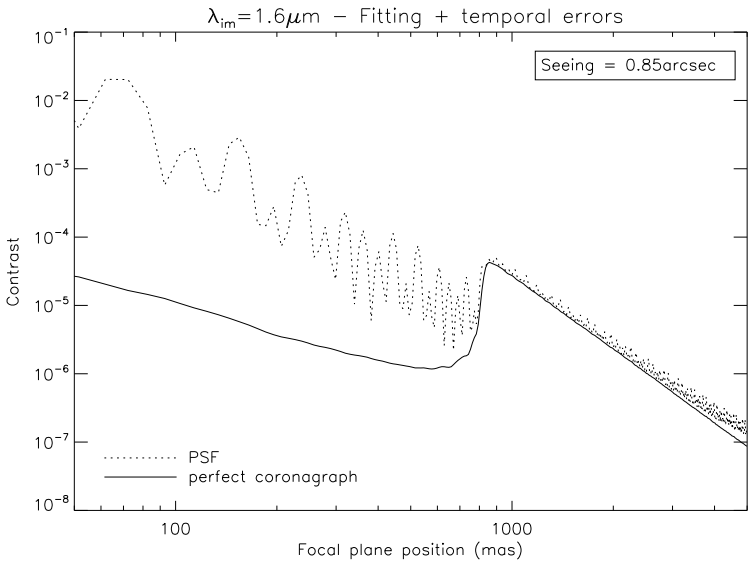


Fig. 2. Comparison of focal plane intensity repartition (expressed in terms of contrast versus the center of the FoV) for AO corrected PSF (without coronagraph) and for a perfect coronagraph, as defined in Eq. (1). The x-axis is in milli-arcsec in the focal plane.

The final performance of the instrument depends on the accuracy of system internal calibrations; that is:

- the calibration of NCPAs [8], the differential aberrations between the two (or more) channels in differential imaging.
- the imperfection of the coronagraphic device itself
- the science detector calibration (flat field), the level of sky background, etc.

Nevertheless, the ultimate limit is given by the photon noise level. In that case, one can show that the total integration time required for achieving a given signal-to-noise ratio (between the planet signal and star residual light) is directly proportional to the shape of $C_{res}$, as shown in Eq. (6):

$$SNR \propto \sqrt{2} * \frac{\sqrt{T_{int} * C_{res}(\rho) * N_s}}{D^2 * S * N_p}, \tag{6}$$

#69303 - $15.00 USD Received 23 March 2006; revised 20 June 2006; accepted 20 June 2006

where $N_p$ and $N_s$ are the numbers of photons per $m^2$ and per s on the telescope pupil for the planet and the star. $S$ stands for the Strehl ratio and $D$ the telescope pupil diameter. It is interesting to note that the integration time decreases as $1/D^4$ for a given contrast.

## 4. Balancing an error budget

The whole AO study is performed with the aim of achieving a balanced error budget.A first approximation (first-order expansion) of this coronagraphic shape is given by the residual phase power spectral density (PSD) as shown in Section 3. Nevertheless, in the coronagraphic shape of the final image, second-order terms can play a non-negligible role depending on the system characteristics (see Subsection 7.1 for instance). Therefore, the global error budget for the AO system has to account for these second error terms, and the global error budget can be summarized as follows:

$$C_{res}(\rho) = \underbrace{C_{scint} + C_{diff} + C_{chrom} + C_{refrac} + C_{aniso}}_{\text{atmospheric limitation}} + \underbrace{\underbrace{C_{fit} + \underbrace{C_{temp} + C_{alias} + C_{noise}}_{\text{low order residual error}}}_{\text{AO loop residual error}} + \underbrace{C_{calib} + C_{aberr}}_{\text{calibration errors}}}. \quad (7)$$

$C_{res}$ is expressed in terms of residual focal position in order to highlight the domains that are affected by each error item. Each error item is described in the following. More generally, the AO error budget can be divided into three main items: atmospheric limitations, AO loop residual errors, and calibration errors. The optimization of this error budget will be performed to meet three main criteria:

- corrected area, i.e., the focal plane area where the image contrast is significantly improved by the AO system. It mainly drives the choice of the number of actuators (the correction area is equal to $\lambda_{im}/d$ in diameter, where $d$ is the actuator spacing). Considering the typical targets that will be observed by SPHERE and the imaging wavelengths ($J$-, $H$-, and $K$-bands), this area has to be larger than 0.8 arcsec in diameter. If a perfect coronagraph is considered, the corrected area can go as close as possible to the optical axis. In practice, a limit will be set by the characteristics and defects of the coronagraph device. For an efficient coronagraph such as the four quadrants phase mask, a reasonable limit should be set around a few (two or three) diffraction angles ($\lambda/D$), which is typically 100 mas for an 8 m telescope in the $H$-band.

- detectivity level, i.e., the capability of the whole system to detect the planet signal. This level is affected by the AO loop errors (temporal, noise, aliasing, etc.), which evolve rapidly with time and can be calibrated using differential imaging and a reference PSF. It can also be degraded by the telescope and the system's high spatial frequencies and NCPAs, which slowly evolve with time and represent the ultimate limitation for the differential imaging and reference PSF subtraction techniques. The minimization of the slowly varying defects implies the measurement and the correction of NCPAs (see Section 8), as well as the stabilization of the optical beam during a whole observation sequence (see Subsection 9.2).

- system sensitivity, i.e., the limiting magnitude of the natural GS used to close the AO loop. This criterion is driven by the number of stars to be observed, but it depends highly on the detectivity level and the corrected area size. Indeed, the larger the corrected area, the smaller the available flux per individual measurement zones (subaperture in the case

#69303 - $15.00 USD Received 23 March 2006; revised 20 June 2006; accepted 20 June 2006

of an SH device, for instance). In addition, increasing the detectivity level implies a reduction in terms of temporal and noise errors, which leads to a faster system working on brighter GSs for wavefront sensing. One can also note that, considering the required level of performance in terms of AO correction, the laser GS solution has been excluded. A first trade-off between scientific goals and system requirements has led to a limiting magnitude of 8 in the *H*-band (corresponding to magnitudes 10–11 for the visible band, depending on the GS types) for the system, implying that the detectivity capabilities have to remain optimum up to this magnitude.

In addition to these three scientific criteria, other constraints have to be taken into account during the instrument design:

- The use of well-proved technologies, if possible.
- New developments for critical issues only, with associated experimental validations.
- A tight schedule (typically 5 years) with finite manpower and budget for building the system.

These last three points are essential for minimizing the risk factor during the instrument realization.

## 5. Simulation tools

Two main classes of simulation tools have been used for the analysis and design of SAXO:

- a PSD-based simulation tool, based on the generalization of an approach first introduced by F. Rigaut and J.-P. Véran [9, 10]. Analytical expressions of spatial PSD are obtained for various errors affecting the AO system (fitting, aliasing, temporal, noise, anisoplanatism, differential refraction, and so on) and used to directly compute AO residual phase screens,
- an end-to-end simulation tool based on a complete and exhaustive (as far as possible) simulation of the AO loop [11]. It includes the Fresnel propagation through the atmosphere (including spherical and laser propagation [12]); an accurate model of the correcting devices (with various influence functions, nonlinear and hysteresis effects, and so on); the Wave Front Sensor (WFS) devices (including diffraction effects, focal plane filtering, chromatism effects, various signal-processing algorithms for both SH and Pyramid); and the control laws (optimal modal gain integrator, Kalman filtering, ... ). The calibration processes are also simulated with their possible error sources (noise, misalignments, NCPAs, and so on).

The PSD-based tool mainly enables rapid reduction of the parameter space in order to make the first system trade-offs [13]. It is also used to feed focal plane instruments (coronagraphs, differential imaging, IFU, etc.) with corrected wavefronts. On the other hand, only an end-to-end model allows for in-depth study of each subsystem behavior and, therefore, the optimization of all the AO parameters (fine design of the WFS, choice of DM characteristics, control law optimization, and so on.).

Using the simulation tools described above, we have studied the effects of all error sources that may degrade the final performance of the AO system. In addition, critical points and news ideas have been validated experimentally by the use of the ONERA AO bench. A short summary of these studies is presented below.

#69303 - $15.00 USD Received 23 March 2006; revised 20 June 2006; accepted 20 June 2006

## 6. Atmospheric limitations

The first kind of error is a gathering of all the propagation effects: scintillation, diffraction, and differential refraction effects. These atmospheric limitations [14] represent the ultimate limitation of a classical AO system, since they cannot be corrected using a single-pupil conjugated DM. The only way to mitigate them is to change the wavefront-sensing wavelength. A more-complete correction of these effects would require a multi-DM system in order to compensate for both phase and amplitude effects. In the following subsection, the different atmospheric effects are studied, and the choice of a classical AO system versus a more-complex multistage AO system is justified.

### *6.1. Scintillation and diffraction effects*

Let us first consider the scintillation and diffraction effects, i.e., the modification of the phase and amplitude of the turbulent wavefront after its propagation through the atmosphere. These effects depend on the turbulence profile ($C_n^2$ profile) and on the wavelength. They affect both the focal plane images [15] (as illustrated in Fig. 3) and the WFS accuracy [16]. Figure 3

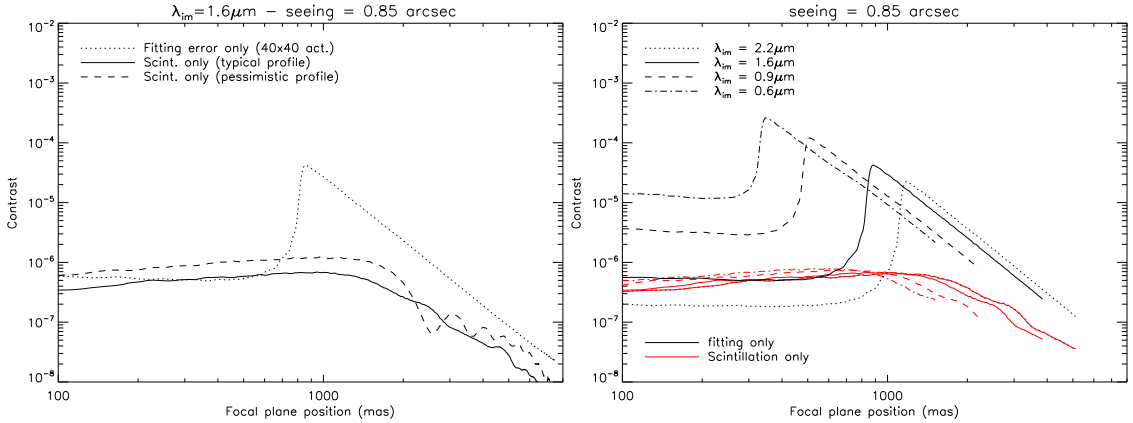


Fig. 3. Comparison of coronagraphic images in the case of a fitting error only (without scintillation error) and in the case of a perfect phase correction but with a scintillation error. [Left] two $C_n^2$ profiles are considered: a typical Paranal case ($\theta_0 = 2.5$ arcsec@$0.5\mu m$) [solid curve] and a pessimistic profile ($\theta_0 = 1.2$ arcsec@$0.5\mu m$). The fitting case [dotted curve] is plotted for comparison. [Right] Effect of the imaging wavelength (from 2.2 to 0.7 $\mu m$). The typical $C_n^2$ profile is considered.

highlights the fact that scintillation effects are negligible in comparison with the residual phase effects, even in the ideal case where only a fitting error is considered (no temporal, noise, or aliasing effects). It also demonstrates that, for a given system (i.e., a given number of actuators) the scintillation effects become more and more negligible (in comparison with phase effects) when the imaging wavelength decreases. The global effects in variance increase in $\lambda^{7/6}$ for scintillation and in $\lambda^2$ for phase effects. Moreover, it is shown that the scintillation effects on the coronagraphic images are barely chromatic in the "corrected area" (wavelength impacts both on the image shape and on the focal plane position in arcsec).

In addition, using a complete Shack–Hartmann (SH) and Pyramid WFS model, it has been shown that the scintillation effects on the WFS accuracy are lower than typically 20 nm rms for a

#69303 - $15.00 USD Received 23 March 2006; revised 20 June 2006; accepted 20 June 2006

pessimistic $C_n^2$ profile and monochromatic wavelength at 0.7 $\mu m$, which is certainly pessimistic since broadband effects will reduce this error.

### *6.2. Chromatism effects on refraction index*

The optical path of the incoming beam through the atmosphere depends on imaging and WFS wavelengths. Indeed, ignoring the effects of humidity and pressure fluctuations, one can express the index fluctuation by the following relation:

$$\Delta n(\lambda) = \left[10^{-6}\left(23.7 + \frac{6839.4}{130-(\lambda)^{-2}} + \frac{45.47}{38.9-\lambda^{-2}}\right)\right]\frac{P}{T^2}\Delta T, \tag{8}$$

with $\lambda$ in microns, $P$ the mean atmospheric pressure, $T$ the mean atmospheric temperature and $\Delta T$ the temperature fluctuations. Note that it is assumed that the index $n$ is equal to

$$n(\lambda) = n_{average} + \Delta n(\lambda). \tag{9}$$

Hence, the difference between the wavefront sensor effective wavelength and the imaging wavelength induces two effects: differential refraction and correction chromatism.

#### 6.2.1. Differential refraction effects

The first effect is due to the wavelength dependency of the refraction index of the atmosphere. Such an effect induces a differential refraction, that is a beam shift for two different wavelengths (each beam propagates in a slightly different part of the turbulence, as shown in Fig. 4). This can be seen as an anisoplanatic degradation: the beam for a given wavelength comes from an equivalent GS position angle of deviation $\theta$:

$$\theta = \left(\Delta n\left[\lambda_{wfs}\right] - \Delta n\left[\lambda_{im}\right]\right) tan\left(zenith\right), \tag{10}$$

with $\Delta n[\lambda]$ the refraction index fluctuations at the wavelength $\lambda$, and *zenith* the zenithal angle. It is therefore clear that the degradation depends on the zenithal angle, the $C_n^2$ profile, the wavefront sensor effective wavelength, and the imaging wavelength. The effects onto the coronagraphic image are illustrated in Fig. 4 for various zenithal angles (right plot). A typical $C_n^2$ profile is considered with a 1.65 $\mu m$ imaging wavelength and a 0.65 $\mu m$ wavefront sensing wavelength. It is interesting to note that the modification of the zenith angle (Fig. 4 [left]) impacts both on the corrected area (due to the differential refraction effects) and on the uncorrected region (due to the increase of the seeing values and thus the fitting errors).

Because differential refraction effects become more and more important when the wavelength difference between imaging and wavefront sensing increases, they will be included in the choice of the WFS wavelength. This trade-off will be made considering that, from a science point of view (number of available targets), SPHERE has to be able to observe up to 40 (with a goal at 50) degrees from zenith.

#### 6.2.2. Chromatism effects on the wavefront correction

The second effect of the difference between imaging and WFS wavelengths is due to the small but yet-existing dependency of the refraction index fluctuations with respect to the wavelength. Hence, the wavefront at a given wavelength $\lambda_1$ is modified with respect to the wavefront at another wavelength $\lambda_0$ by the relation:

$$\phi_{turb}(\lambda_1) = \frac{\Delta n(\lambda_1)}{\Delta n(\lambda_0)}\phi_{turb}(\lambda_0). \tag{11}$$

#69303 - $15.00 USD Received 23 March 2006; revised 20 June 2006; accepted 20 June 2006

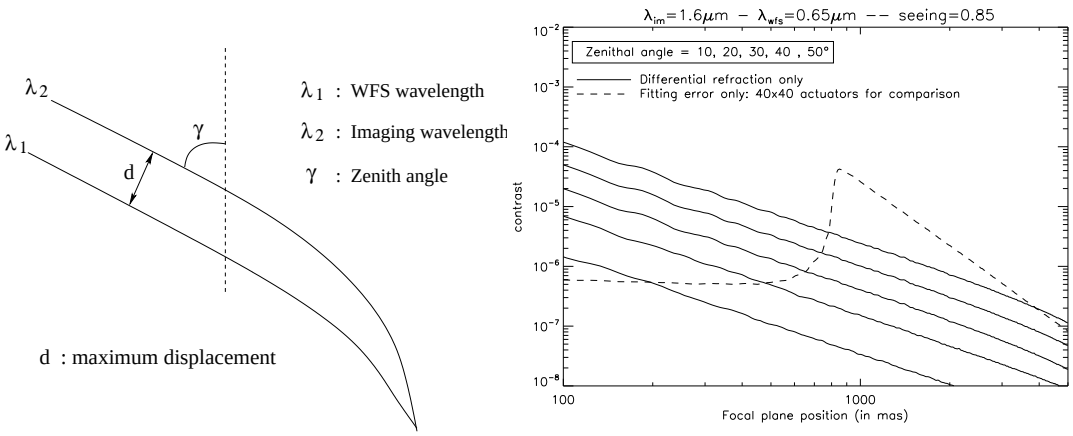


Fig. 4. [Left] Schematic representation of the differential refraction effect. [Right] Influence of the zenith angle for a $1.65\mu m$ imaging wavelength and a $0.65\mu m$ WFS wavelength (a perfect correction at WFS wavelength is assumed in each case). A typical $C_n^2$ profile has been considered. The fitting error of a 40x40 subapertures system has been plotted for comparison).

Because the correction provided by the DM is proportional to $n(\lambda)$ and not to $\Delta n(\lambda)$, the correction phase obtained from $\lambda_0$ measurements and expressed at the $\lambda_1$ wavelength is equal to

$$\phi_{corr}(\lambda_1) = \frac{n(\lambda_1)}{n(\lambda_0)}\phi_{corr}(\lambda_0). \tag{12}$$

Hence, even if the turbulence is perfectly measured and corrected at one given wavelength, the residual wavefront for another wavelength is not null and is directly proportional to the input signal itself, with an attenuation coefficient depending on the index values for the two wavelengths:

$$\phi_{res}(\lambda_1) = \phi_{turb}(\lambda_1) - \phi_{corr}(\lambda_0) \simeq \frac{(\alpha-1)}{\alpha}\phi_{turb}(\lambda_1), \tag{13}$$

where $\alpha = \Delta n(\lambda_1)/\Delta n(\lambda_0)$. Therefore, the coronagraphic error term induced by the chromatism error on wavefront correction is directly proportional to the turbulent power spectral density, that is, with a $\rho^{-11/3}$ dependency at least for $\rho$ larger than a few tens of arcseconds (not affected by outer scale effects). The proportionality coefficient is equal to $(\alpha-1)^2/\alpha^2$. It is interesting to mention here that this effect is fully predictable (if average atmospheric parameters T and P are known). It can be included in a control law scheme in order to dramatically reduce its effects.

Nevertheless, as shown in Fig. 5, error remains negligible in comparison with differential refraction effects at least in the inner working area (between 100 and 3000 mas). The conclusion is surely different if a larger telescope is considered. In that case the diffraction pattern becomes smallerm and one would want to work closer to the optical axis where the chromatism effects cannot be neglected anymore. In that case a modification of the control law should be required to compensate for the chromatism effects.

#69303 - $15.00 USD Received 23 March 2006; revised 20 June 2006; accepted 20 June 2006

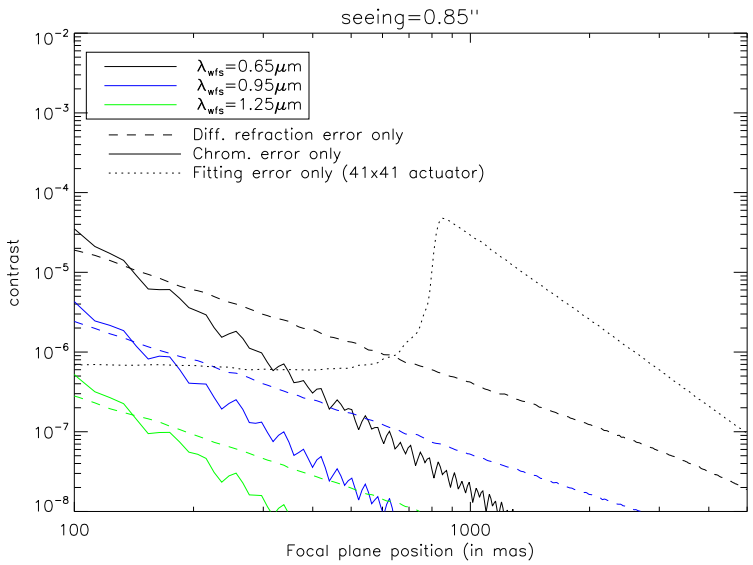


Fig. 5. Impact of the WFS wavelength on chromatic errors (differential refraction and wavefront correction). The imaging wavelength is $1.6\mu m$. The Zenith angle is equal to $40^o$. A typical $C_n^2$ profile has been considered (a perfect correction at WFS wavelength is assumed in each case). The fitting error of a 40x40 subapertures system has been plotted for comparison).

### *6.3. Conclusion in terms of system design*

Full correction of scintillation effects would only lead to an equivalent reduction of the phase variance smaller than 20 nm rms. In comparison with the small gain in performance, the system complexity is highly increased (two DMs, measurement devices, reconstruction process, calibration issues, etc.). In consideration of the small expected gain, even if the scintillation were fully corrected (which is far from being manifest), it has been decided not to consider a scintillation corrector for the SAXO system. It has been shown that the main limitation in terms of atmospheric errors would be the differential refraction rather than scintillation. In that case, the ways to mitigate these effects would be a modification of the WFS wavelength in order to be as close as possible to the imaging wavelength, or to limit the portion of accessible sky (observe only close to zenith).

## 7. AO loop residual errors

The AO loop residual errors gather all the errors related to the AO system itself. These errors can be divided in two main types: high-order errors, which affect the high spatial frequencies only, i.e., mainly the focal plane area located far from the optical axis ($> \lambda/2d$, with $d$ the interactuator distance); and low-order errors, which affect the low spatial frequencies–mainly the focal plane area located close to the optical axis.

### *7.1. Fitting error*

Concerning the top level specifications for SPHERE, the minimization of the global error budget is not the only pertinent criterion; the spatial repartition of the errors also has to be taken into account. In particular, the detectivity performance is also linked to the capability of the AO

#69303 - $15.00 USD Received 23 March 2006; revised 20 June 2006; accepted 20 June 2006

system to "clean up the PSF" (i.e., to be as close as possible to the diffraction pattern) in an area wider that 150 arcsec around the optical axis. This corrected area (corr) in the focal plane (see Fig. 6) is directly linked to the interactuator distance ($d = D/(n_{act} - 1)$, where $n_{act}$ is the linear number of actuators in the telescope diameter $D$) with the following relation: corr = $\lambda_{im}/2d$. In that case, the residual phase power spectral density (PSD) is equal to 0 in the $0 - \lambda/2d$ frequency domain. Nevertheless, when a coronagraphic image is consider, the approximation coronagraphic image equal the phase PSD is only valid in a first order approximation (the classical approximation $e^{i\varphi} \simeq 1 + i\varphi$). When a general coronagraphic image formation is considered, the second-order terms of this approximation can no longer be neglected. Their effect is nothing but a spread of the residual uncorrected phase in the whole focal plane (see eq. (7) and Ref. [17]). It induces a plateau in the focal plane domain for small separation (between 0 and $\lambda/2d$, that is, in the corrected area). Therefore, decreasing $d$, i.e., increasing the number of actuators, reduces the low-frequency plateau on the coronagraphic image.

Nevertheless, decreasing $d$ has some consequences in terms of the system limiting magnitude. Indeed, the larger the number of DM actuators is, the larger the number of WFS subapertures and, hence, the smaller the number of available photons per subaperture and per frame becomes.

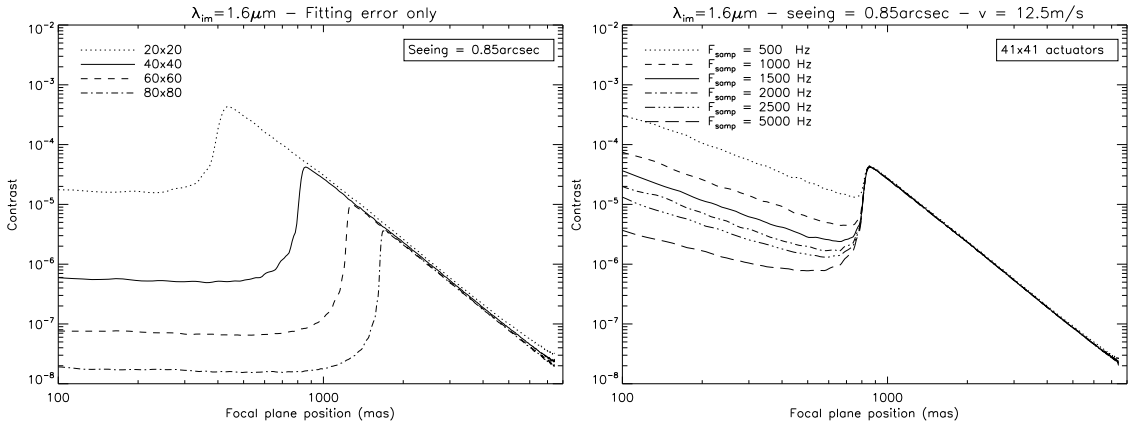


Fitting error Temporal error

Fig. 6. [Left] Effect of the number of actuators on the coronagraphic image. Four actuator grids (20x20, 40x40, 60x60 and 80x80) have been considered. The imaging wavelength is set to 1.65 $\mu m$. Only the fitting error is considered. [Right] Effects of temporal errors on the coronagraphic images. Only atmospheric perturbations are introduced (no vibrations). The average wind speed is equal to 12.5 m/s.

Concerning the science goals and all the error sources, a 40 x 40 actuator DM is a good compromise in terms of corrected area size, detectivity issues, and system limiting magnitude. In addition, such a number of actuators can be achieved by using well-known piezo-stack technologies with the required performance in terms of actuator and interactuator strokes (to correct for turbulence and system phase defects), bandwidth (higher than a few kHz), hysteresis (a few percent), etc. A larger number of actuators would require the use of microdeformable mirrors. Even if these promising technologies are in widespread development, they represent an important risk for a fast track system (less than 5 years). The use of existing (or soon-to-be) technologies would imply a woofer–tweeter configuration (one DM for low spatial frequency

#69303 - $15.00 USD Received 23 March 2006; revised 20 June 2006; accepted 20 June 2006

correction, another for high frequency correction), which represents a non-negligible risk from a system point of view that includes calibration issues, ultimate performance of the device, side effects, and so on.

### *7.2. Temporal error*

Another important item is the temporal error. Its behavior is dependent on turbulence characteristics and on each AO component: detector integration time, readout noise, real-time computations of commands from WFS data, numerical corrector, digital–analog converter, high voltage amplifier, and DM actuator temporal response.

Choosing the temporal sampling frequency results in trade-offs among the following:

- the atmospheric turbulence to correct for (seeing and wind speed). The system bandwidth, which can be defined as $F_{samp}/12.5$ (for maximum gain under stability and robustness constraints [18] and for a two-frame-delay system), has to be larger than the turbulence temporal evolution of the faster mode to be corrected.

- the expected limiting magnitude of the whole system (detectivity issues and trade-offs between measurement noise and temporal effects); the higher the sampling frequency, the lower the limiting magnitude.

- the system parameters (detector technologies, correcting devices, real time computer performance).

- the telescope and system vibration issues. With a classical integrator law, the correction of vibrations requires a system bandwidth much larger than the vibration frequency. This may be an extremely tight specification and may be incompatible with the limiting magnitude requirements. Another (and optimal way) to deal with all these parameters (for a given sampling frequency) is to design a Kalman-filter–based control algorithm [19]. Nevertheless, practical implementation of such a control law is complex and requires more computing power, especially for high-order systems. This leads to a significant increase of the RTC complexity. A hybrid solution has been considered for dealing with this problem. An optimal modal gain integrator [20] has been chosen to control high-order modes while a Kalman filter will be considered for tip-tilt modes to optimally correct turbulence and vibration effects.

Figure 6 (right) shows the evolution of the coronagraphic image as a function of the temporal frequency of the WFS device. A two-frame delay is considered (one for the detector integration and one for the detector read-out and voltage computation) along with a classical integrator law.

### *7.3. Aliasing error*

These effects are the result of high spatial frequencies that are seen as low ones by the WFS device. The uncorrected high-frequency signal is translated in low-frequency measurements by the WFS device itself. These aliased high-frequency measurements are added to the real low-frequency signal and thus induce a measurement error. Therefore this aliasing error is directly linked to the fitting error (the greater the residual uncorrected signal, the larger the aliasing effects). It dramatically increases the PSF residuals in its corrected area (because, as explained before, aliasing effects translate uncorrected high-frequency signals in low-frequency errors). Of course the total amount of error depends on the WFS concept. As an example in the specific case of classical SH WFS, it corresponds to roughly 40% of the total fitting error variance. Some aliasing-free focal plane sensors have been proposed to significantly reduce these effects (see Fig. 7). One of them is the spatially filtered SH, proposed by Poyneer and Macintosh

#69303 - $15.00 USD Received 23 March 2006; revised 20 June 2006; accepted 20 June 2006

[21, 22]. It is based on a focal plane filtering before the wavefront sensing device. The filtering process is performed using a pinhole device located in a focal plane before the SH lenslet array. This device has been studied in depth and optimized with respect to the system and turbulence characteristics (spectral bandwidth, WFS sampling, turbulence, etc.). Its optimal size ranges between 0.85 and 1.6 arcsec, typically. In addition, an experimental validation of the concept has been conducted using the ONERA AO bench (see Ref. [23]) in closed loop and with turbulence. The gain brought by a filtering device has been clearly demonstrated, and the experimental results have been found in good agreement with the simulations, which validates the potentiality of the concept and its use in the SAXO design.

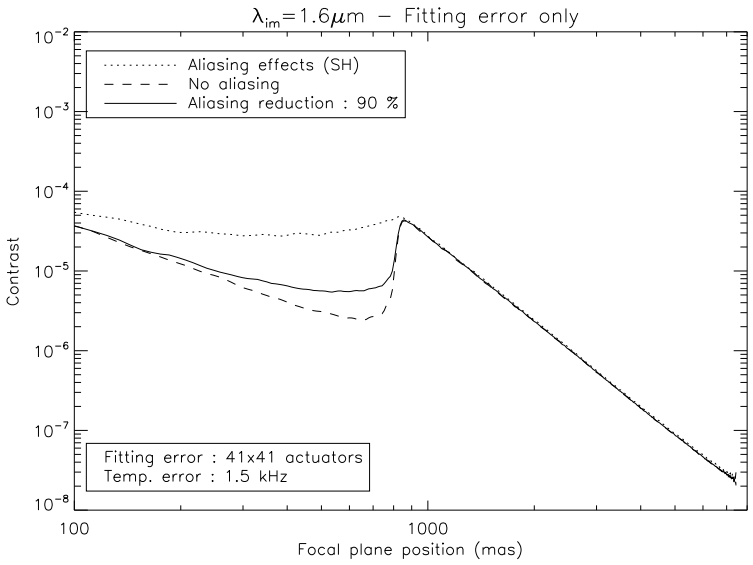


Fig. 7. Impact of aliasing effects on coronagraphic images. The case of a classical SH, a spatially filtered SH, and an aliasing-free WFS have been considered.

### *7.4. WFS measurement error*

#### 7.4.1. WFS wavelength

The choice of the analysis wavelength is based on the available number of photons in a given spectral range (it is therefore linked to the GS type, as shown in Fig. 8 [left]) and on the detector characteristics. These two points allow us to compare WFS noises. Without any other consideration, it is interesting to note that the number of available photons becomes more important in IR bands only for very red stars (typically later than M5).

A global comparison has been made between IR and VIS WFS. The main advantages and drawbacks of each type of WFS are summarized below.

- IR-WFS
  - Advantages: (1) no differential refraction between WFS and imaging path and smaller scintillation effects on the WFS, inducing an increase of the overall system performance at very high flux and leading to a simpler system (only one ADC at the entrance for the system, which can be seen and corrected by the AO loop); (2) accessibility to faint red targets (M5 and redder).

#69303 - $15.00 USD Received 23 March 2006; revised 20 June 2006; accepted 20 June 2006

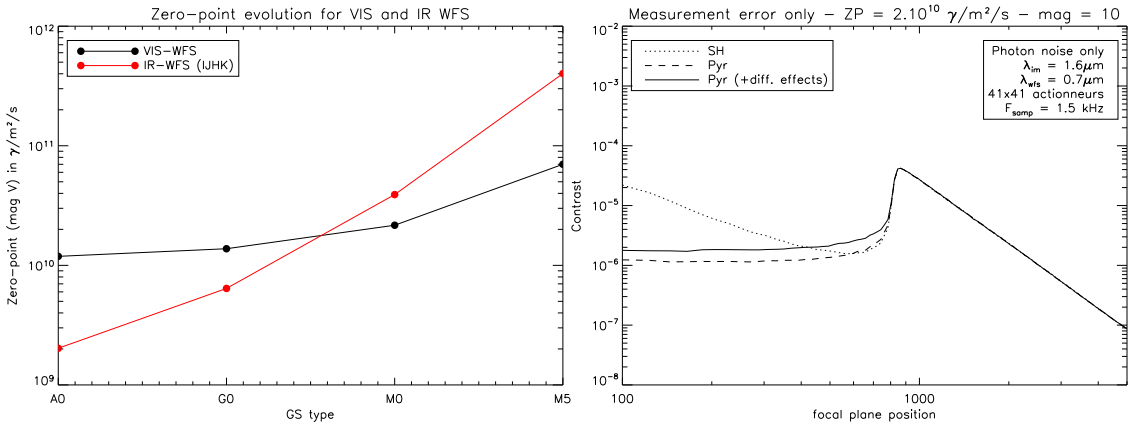


Fig. 8. [Left] Comparison of system zero-points for various GS types and assuming an IR or a VIS-WFS. [Right] Comparison of coronagraphic images in the case of a Pyramid (perfect and with diffraction effects) and a SH WFS.

  - Drawbacks: (1) lower flux for GS up to M5 (decrease of the number of accessible targets); (2) flux separation between WFS and scientific paths (need for several beam splitters optimized for each scientific instrument purpose); (3) increase of system complexity; (4) need for a complex cryostat; (5) high RON values for high frame rates; (6) high background noise; (7) complex detector calibration (cosmetics, etc.).

- VIS-WFS
  - Advantages: (1) gain in sensitivity (in $\left(\lambda_{im}/\lambda_{wfs}\right)^2$, i.e., a factor 8 between 2 and 0.7 $\mu m$); (2) no flux separation (all the VIS photons are available for WFS); (3) low RON level (even close to 0 for new EMCCD technologies); (4) very low background noise ($>$ 22 mag/arcsec$^2$).
  - Drawbacks: (1) differential refraction effects (i.e., limitation to zenith angles smaller than 50$^o$); (2) scintillation effects on WFS; (3) limited access to faint red targets; (4) two ADC in the two separated paths.

With consideration given to the system requirements and the VLT-PF targets, the choice of a VIS-WFS has been made, with a spectral bandwidth going from 0.45 to 0.95 $\mu m$. This choice assumes that an EMCCD with read-out noise lower than 1 e- at 1.5 kHz will be available in time. The development of such a device has been funded by the European Community (FP6-Opticon Program), and a first detector should be available within the next two years.

#### 7.4.2. Pyramid versus SH

A comparison of the SH and Pyramid WFS in the frame of the VLT-PF AO system has been conducted. In both cases, performance, required calibrations and optimizations, as well as fundamental limitations have been identified and quantified. Theoretically, i.e., without modulation and with its expected noise propagation terms (as shown in Fig. 7 [left]), the Pyramid WFS provides a better shape of the coronagraphic image. Nevertheless, more accurate end-to-end simulations have identified some yet unsolved problems concerning the Pyramid WFS. In particular,

#69303 - $15.00 USD Received 23 March 2006; revised 20 June 2006; accepted 20 June 2006

in a partial correction domain (case of a visible WFS), the pattern structure introduces a "natural" modulation that evolves with time, introducing a variability of the linearity coefficient of the WFS sensor and then a corresponding gain fluctuation of the global AO loop. To overcome this effect, an instrumental modulation must be introduced, which will affect the propagation terms and thus make the Pyramid results comparable (and even poorer for medium-to-bad atmospheric conditions) to those of the SH.

Hence considering the WFS performance, stability, complexity, and risk evaluation, a spatially filtered SH WFS, combined with a new optimized slope estimation algorithm [24], has been chosen as a baseline for the SAXO system. It allows us to reach a limiting magnitude of approximately 10-11, depending on GS type and CCD performance [22].

## 8. Calibration errors

The calibration errors [25] gather the AO loop (interaction matrix [IM] and reference slopes) and NCPA miscalibrations.

### *8.1. AO calibration*

The effects of misalignment on system performance have been studied, leading to tight specifications on system stability (pupil conjugation between DM and WFS, pupil motion, noise of IM, and reference slopes measurements, among other things). To illustrate, Table 1 shows the impact of a misregistration between DM and WFS, i.e., a differential pupil shift between these two components.

Table 1. Impact of pupil shift between DM and WFS.

| Pupil Shift between DM and WFS (in sub-aperture %) | 5 | 10 | 15 | 20 | 25 |
|---|---|---|---|---|---|
| error in nm rms | 4 | 9 | 15 | 23 | 32 |

This effect is critical in terms of system performance. To avoid it, in the SAXO optical design both DM and TTM are located in a pupil plane, and there are no moving optics located outside the pupil between the DM and the WFS.

To reduce noise effects on IMs, we will consider Hadamar approaches [26] for IM measurements.

### *8.2. Calibration of NCPAs*

Each NCPA will be measured using a phase diversity approach and corrected in a closed-loop scheme through a modification of the WFS references [27, 8]. A detailed global analysis has shown that correcting an NCPA is mandatory for achieving the contrast goals. Of course, the low-order modes are critical, and the error budget balance leads us to consider only the precompensation of, typically, the first 100 modes. These modes have to be corrected with an accuracy of less than 10 nm rms (that means less than 1 nm per mode).

An example of the optimized procedure developed at ONERA and applied on our AO bench (BOA) is proposed in Fig. 9. Twenty-five Zernike coefficients have been measured by using phase diversity on the imaging camera, and precompensated through the modification of the WFS reference slopes by using an iterative process to account for uncertainties on the WFS model. The residual wavefront error on the corrected static aberration is smaller than 2 nm rms with such a procedure. It can be noticed that next 50 uncorrected Zernike coefficients have a

#69303 - $15.00 USD Received 23 March 2006; revised 20 June 2006; accepted 20 June 2006

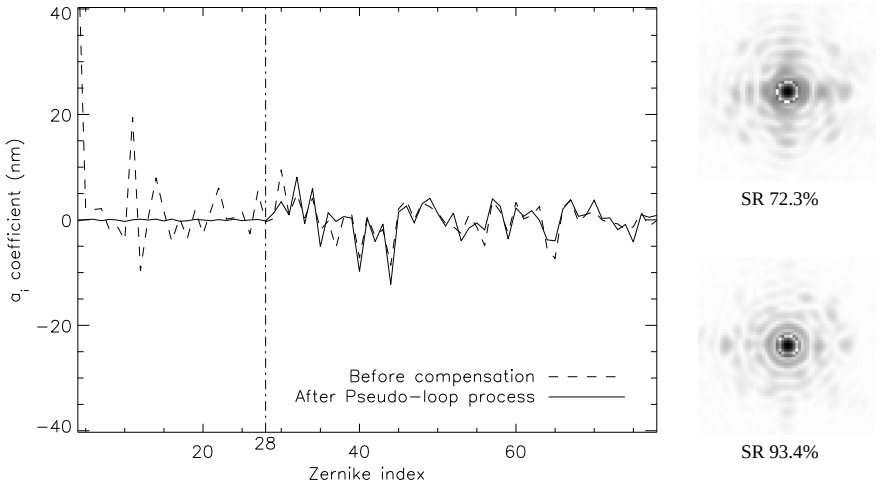


Experimental validation of the NCPA measurement and precompensation process

Fig. 9. [left] Wavefront error of static aberration on the ONERA AO bench before and after measurements and precompensation. Twenty-five Zernike polynomials have been measured and precompensated. [Right] PSF before and after precompensation. The SR goes from $72 \pm 2\%$ up to $93 \pm 2\%$ at 633 nm.

total rms error of 25 nm, which is fully coherent with the SR estimation made directly on the image (93% at 633 nm, see Fig. 9).

## 9. Auxiliary devices

### *9.1. IR tip-tilt sensor*

The average image position (in other words, the optical axis position) on the coronagraphic mask is a main specification for the VLT-PF system. The required accuracy for the mean image position is 0.5 mas or better. The global error for the image position depends on the following:

- the residual uncorrected tip-tilt fluctuations at very high frequency (considered here as a noise). From the AO residual errors, these fluctuations have to be lower than 2 mas (at 1 kHz frame rate). Considering a 100 ms integration time, this leads to a residual error of 0.2 mas;
- the differential refraction effect (between VIS and IR wavelengths). Such an effect has been estimated to 0.16 mas per second in the more pessimistic case of a 60 degrees zenith angle;
- the differential thermal or mechanical effects (between WFS and imaging paths). Such effects have been estimated to 0.031 mas per second.

Considering the requirement, we believe that an open-loop model of each differential evolution will not be accurate enough (considering all the possible parameters involved) to reach the absolute position performance. As an example, a 10% error on the model will lead to a residual shift of the mean image position of 0.02 mas per second; and therefore, the specification can be kept only for 25 s of observation time.

#69303 - $15.00 USD Received 23 March 2006; revised 20 June 2006; accepted 20 June 2006

To ensure that the specification will be fulfilled, an auxiliary IR tip-tilt sensor (AS) at the level of the coronagraphic mask has been proposed. This sensor will be coupled with a differential tip-tilt mirror (DTTM) located in a pupil plane in the WFS arms. The auxiliary loop can be summarized as follows: (1) image acquisition with AS (typically 10 Hz); (2) computation of residual image motion from AS data; (3) application of DTTM voltages from AS data; and (4) the differential motion induced by the DTTM is seen by the VIS-WFS and thus corrected by the main tip-tilt mirror, which leads to an image recentering on the coronagraphic mask.

### *9.2. Pupil motion sensor*

Pupil stability is a major issue in ensuring the VLT-PF performance. The pupil must remain motionless during the entire observation process. When the pupil is located behind the Nasmyth focus of the telescope, this stability requirement implies a pupil derotator and a pupil recentering device. It has been shown on simulations that a pupil shift of 1% of the pupil diameter or a pupil rotation of 1 degree will reduce by a factor of 1.5 to 2 (for typical conditions at the VLT) the detection capability of a coronagraphic + differential imaging system. It has led to impose

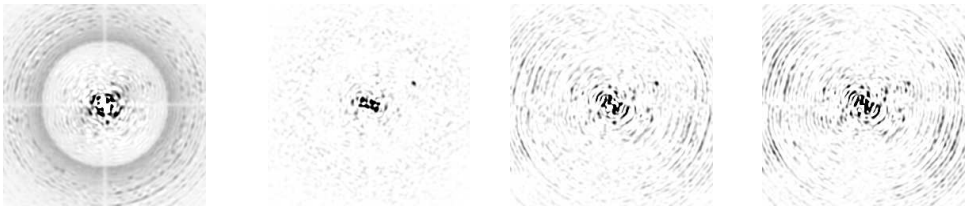

differential image | motionless pupil | pupil motion = 0.6% | pupil motion = 1.2%

Differential image + calibration on reference star

$I(\lambda_1) - I(\lambda_2)$ | $[I(\lambda_1) - I(\lambda_2)] - [Ref(\lambda_1) - Ref(\lambda_2)]$

Fig. 10. [Left] Differential coronagraphic (4-quadrant) image ($\lambda_1 = 1.56\mu m$, $\lambda_2 = 1.59\mu m$). [Right] differential coronagraphic image + reference subtraction: pupil shift between object and reference star = 0, 0.6, and 1.2 % of the full pupil. The companion ($\Delta_m = 15$, separation = 0.6 arcsec) is clearly distinguishable from residual fixed speckles for a fixed pupil.

a pupil stability in translation better than 0.2% (goal 0.1%) of the full VLT pupil. This performance is achieved using a pupil tip-tilt mirror located close to the entrance focal plane of the VLT-PF. This mirror is controlled by a pupil motion sensor (PMS). The PMS directly uses the SH-WFS data to measure pupil motion. Because pupil motion is rather slow, a measurement-correction process has to be performed typically every minute, which ensures a good SNR on the PMS data.

## 10. Global system design

A global trade-off from all the points mentioned above (combined with optical design, technological aspects, cost, and risk issues) leads to the following main characteristics of the AO system:

- 41x41 actuator DM (roughly 1300 useful actuators) of 180 mm diameter, located in a pupil plane with an interactuator stroke $> \pm 1\mu m$ (mechanical), a maximum stroke $> \pm 3.5\mu m$ (mechanical), and a temporal transfer function phase shift lower than $5^o$ at 80 Hz.

#69303 - $15.00 USD Received 23 March 2006; revised 20 June 2006; accepted 20 June 2006

- 2-axis TTM (70 mm diameter) located in a pupil plane, with a resolution of $\pm 0.5$ mas and a transfer function phase shift lower than $8^o$ at 80 Hz.
- 40x40 SH WFS with a spectral range covering 0.45 to 0.95 $\mu m$; 6x6 pixels per subaperture (Shannon sampling @ 0.65 $\mu m$); a focal plane filtering device with variable size (from $\lambda/d$ to $3\lambda/d$ at $0.7\mu m$); and a temporal sampling frequency of 1kHz (goal 1.5 kHz). The foreseen detector is a 256x256 pixels Electron Multiplication CCD detector with a read-out-noise $< 1e^-$ and a 1.4 excess photon noise [28, 22].
- Mixed numerical control laws with a Kalman-filter law for tip-tilt control and an optimal modal gain integrator law for DM control. The global AO loop delay has to be lower than 1 ms (goal 666 $\mu s$).
- NCPAs with off-line measurements and on-line compensation using a phase diversity algorithm and an on-line modification of the WFS reference slopes.
- Pupil motion sensor that uses SH data directly (no additional sensor) and controls a slow (typically lower than 1 Hz) tip-tilt mirror located near the system entrance focal plane.
- Auxiliary IR tip-tilt sensor and associated differential tip-tilt mirror located in a pupil plane on the WFS arm. This auxiliary sensor corrects for optical axis position and should allow an average position of the optical axis with respect to the coronagraphic device better than 0.5 mas (for optical axis fine centering).

## 11. Conclusion

The SAXO system, but more generally any AO system for a planet finder instrument, represents a large step forward with regard to system components and calibration procedures. Nevertheless, a complete analysis with a detailed error budget has shown that an AO system fulfilling all the requirements that are mandatory for the direct detection of giant extrasolar planets is feasible on a reasonable time scale (4 years) and with existing and proven technologies. The realization of the SPHERE instrument is a critical step toward a future 30- to 60-m Extremely Large Telescope (ELT), both from the conceptual and a technological points of view. The next steps will be the realization of the first AO systems for ELT (foreseen to be within 10–15 years), and on a larger time scale (probably the second generation of ELT instrumentation), the realization of a planet finder instrument for these telescopes with the ultimate goal of the direct imaging of an extrasolar terrestrial planet.

## Acknowledgments

The authors warmly thank all the members of the SPHERE consortium for their contributions to this study. ONERA and LESIA will be involved in the development of the SAXO system in the frame of the newly established “Groupement d’Intêret Scientifique” PHASE.

#69303 - $15.00 USD Received 23 March 2006; revised 20 June 2006; accepted 20 June 2006